Promotion Mechanisms of Au Supported on TiO_2 in Thermal- and Photocatalytic Glycerol Conversion

Yanbin Shen,[†,‡,¶] Aref Mamakhel,[§] Xi Liu,[‡] Thomas W. Hansen,[∥] Tommaso Tabanelli,[⊥] Danilo Bonincontro,[⊥] Bo B. Iversen,[§] Laura Prati,[#] Yongwang Li,[‡] J. W. Hans Niemantsverdriet,[‡,▽] Graham Hutchings,[○,◆] Nikolaos Dimitratos,[⊥,○,◆] Alberto Villa,[*,#,○] and Ren Su[*,†,‡]

[†]Soochow Institute for Energy and Materials InnovationS (SIEMIS), Key Laboratory of Advanced Carbon Materials and Wearable Energy Technologies of Jiangsu Province, Soochow University, Suzhou 215006, P. R. China

[‡]SynCat@Beijing, Synfuels China Technology Co. Ltd., Beijing 101407, China

[§]Center for Materials Crystallography, Department of Chemistry and iNANO, Aarhus University, DK-8000 Aarhus C, Denmark [∥]DTU Nanolab, Technical University of Denmark, DK-2800 Kgs. Lyngby, Denmark

[⊥]Dipartimento di Chimica Industriale "Toso Montanari", Universitaédi Bologna, Viale del Risorgimento 4, 40136 Bologna, Italy

[#]Dipartimento di Chimica, Universitaédegli Studi di Milano, via C. Golgi 19, 20133 Milano, Italy [▽]SynCat@DIFFER, Syngaschem BV, 5600 HH, Eindhoven, The Netherlands

. The UK Catalysis Hub, Research Complex at Harwell, Oxfordshire OX11 0FA, U.K.

Cardiff Catalysis Institute, Cardiff University, Cardiff CF10 3AT, U.K.

* Supporting Information

ABSTRACT: Catalytic glycerol conversion by means of either photon or thermal energy is of great importance and can be realized by metal supported on TiO_2 systems. Although various procedures have been employed to synthesize efficient metal/TiO_2 catalysts, the promotional mechanisms for both reactions are still unclear due to the lack of well-defined systems. Here, we have deposited gold nanoparticles on a series of highly crystalline anatase TiO_2 substrates with different crystallite sizes (7, 12, 16, 28 nm) by both direct precipitation and sol-immobilization methods to examine the effect of metal deposition methods and TiO_2 sizes on both photo- and thermal catalytic glycerol reforming. For photocatalytic H_2 evolution from glycerol, optimum performance was observed for the Au supported on 12 nm TiO_2 for both deposition methods. For thermal catalytic glycerol oxidation, all catalysts show a similar selectivity to glycerate (>70%) regardless of the TiO_2 size and metal deposition method; however, the metal deposition method significantly influences the catalytic activity. In situ UV−vis spectrometry reveals that the optimized photocatalytic performance originates from enhanced charge transfer kinetics and a more negative Fermi level for proton reduction, whereas electrochemical analysis reveals that the promoted glycerol oxidation is caused by the enhanced oxygen reduction half-reaction.

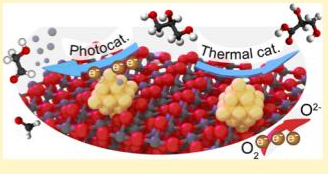

INTRODUCTION

Biomass-derived polyols have been recognized as feedstocks for the production of pharmaceuticals, polyethers, and foods.[1−3] Efficient conversion of polyols to these value-added products by means of catalysis has attracted huge interest for decades.[3−5] For example, the utilization of glycerol as a versatile building block for the synthesis of chemicals and fuels via thermal and photocatalysis has been extensively inves-tigated,[6−10] as biodiesel production has increased drastically in recent years in which glycerol is an abundant by-product (10 wt %).[11]

As a highly functionalized molecule consisting of three hydroxyl groups, a range of products can be synthesized from glycerol via thermal catalytic oxidation using designed catalysts.[12,13] The most commonly used catalysts for glycerol oxidation are noble-metal-supported nanoparticles (NPs). It has been shown that the use of supported monometallic (Au, Pd, Pt) and bimetallic (Au-Pd, Au-Pt) NPs shifts the selectivity to glyceric acid and tartronic acid with improved stability and activity, whereas the addition of Bi to the noble metal NPs enhances the selectivity in glycerol oxidation to dihydroxyacetone.[14,15] Besides, the particle size, oxidation state, microstructure of metal NPs, and nature of the support (porosity, acid−base properties) can also be used to regulate the activity and selectivity in glycerol oxidation.[16] Moreover, the selective oxidation of glycerol under base-free reaction conditions has enabled new pathways for the production of value-added products.[17,18]

Meanwhile, hydrogen production via photocatalytic glycerol reforming under UV or solar irradiation under ambient

conditions has been also investigated and is considered as a promising green energy source.[19,20] In order to overcome the low quantum efficiency of pristine photocatalysts, incorporation of various semiconductor heterojunctions and metal−semiconductor interfaces has been widely explored.[21−23] It has been reported that engineering the size, microstructure, and chemical composition of the promoters and the semiconductor support all influences the charge transfer kinetics of the photogenerated charge carriers, resulting in significant variations in the H_2 production rate.[21,24,25] A mechanistic study on noble-metal-modified TiO_2 reveals that photoreforming of glycerol mainly occurs via the oxidative C−C cleavage, resulting in the formation of glycolaldehyde and formaldehyde as the dominant products (61%).[10] Meanwhile, the oxidation of primary or secondary carbon leads to the formation of glyceraldehyde (26%) or dihydroxyacetone (13%), respectively. Similar results are also observed for other metal NP (i.e., Pt, Cu, Ni)-decorated TiO_2.[19]

Although thermal and photocatalytic glycerol reforming processes are performed under different conditions, noble metal NPs supported on semiconductors (i.e., TiO_2, CuO, NiO_x) are widely used as catalysts for both processes.[26−31] Note that both thermal and photocatalytic glycerol conversions are oxidative reactions but performed under different reaction conditions. While the thermo-process is performed under aerobic conditions with heat as the energy source, the photoprocess takes place under deaerated conditions initiated by photon energy. This also results in a difference of dehydrogenation products: water and molecular hydrogen for thermal and photocatalytic glycerol reforming, respectively. While the noble metal NPs are the active species in the thermal catalytic process,[13,32] the metal NPs are generally considered as cocatalysts and electron reservoirs for controlling charge transfer in the photocatalytic process.[25,33] However, it should be noted that electronic and geometric effects of the semiconductor support and the interaction between the metal NPs and the support will also influence the thermal and photocatalytic glycerol reforming performance. It has been reported that the selectivity and turnover frequency (TOF) of metal NPs in glycerol oxidation can be controlled by tuning the identity of the support.[34] Meanwhile, we have shown that the type of photogenerated radical on the surface of Pd/TiO_2 depends on the crystallite size of anatase TiO_2.[35]

In order to improve the catalytic performance, various metal deposition methods (i.e., sol-immobilization, precipitation, vapor deposition) have been employed to modify a variety of semiconductor supports.[13,36] It is generally considered that the enhanced catalytic performance of some catalysts is related to a smaller particle size and homogeneous distribution of the metal NPs.[37,38] However, contradicting results have also been reported on the medium and large metal NPs.[39,40] Previous electrochemical analysis shows that both the activity and selectivity in glycerol oxidation are strongly dependent on pH and the catalyst; however, these results are based on metal single-crystal electrodes, and thus, the effect of the support has been ignored.[32,41] This indicates that the promotional effect of metal NPs in both thermal and photocatalytic glycerol reforming still needs to be investigated using well-defined systems and in situ techniques.

Here, we report how the TiO_2 support size and the metal deposition methods influence the photocatalytic H_2 production from glycerol and thermal catalytic glycerol oxidation. In order to realize this, we have synthesized a series of highly crystalline anatase TiO_2 NPs with well-defined crystallite sizes ranging from 7 to 28 nm, which were then loaded with Au NPs via the direct precipitation or sol-immobilization method. We used in situ UV−vis spectroscopy and electrochemical analysis to probe the promotion effects.

EXPERIMENTAL SECTION

Synthesis and Characterization of Photocatalysts. Synthesis of TiO_2 Particles. Highly crystalline TiO_2 powders with different crystallite sizes were prepared via a supercritical synthesis approach by employing a continuous flow reactor.[42] The supercritical solvent and the reactant are isopropanol mixed with deionized (DI) water and titanium isopropoxide (TTIP, ACROS, 98%), respectively. By tuning the solvent composition, flow rate, reaction temperature, and pressure, anatase TiO_2 particles with averaged crystallite sizes of 7, 12, 16, and 28 nm were synthesized, as listed in Table S1 in the Supporting Information.[43] After the reaction, the suspensions containing as-prepared TiO_2 particles were centrifuged, washed with DI water, and dried overnight at 120 °C.

Deposition of Au NPs on TiO_2. Both direct precipitation (DP) and sol-immobilization (SI) methods were utilized to deposit 1 wt % Au NPs on the aforementioned anatase TiO_2 particles. For the DP deposition, the TiO_2 powders were first dispersed in DI water (~10 mg L^{-1}). Then a $NaAuCl_4$ solution (43 μmol of $NaAuCl_4 \cdot 2H_2O$) was added to the suspension together with urea under vigorous stirring. The catalyst was filtered, washed three times with DI water, then suspended in DI water, and subsequently reacted with a freshly prepared $NaBH_4$ solution (0.1 M, n[$NaBH_4$]/n[Au] = 4) under vigorous stirring at room temperature (RT). The sample was filtered, washed, and dried at 80 °C for 4 h. For the SI deposition, solid $NaAuCl_4 \cdot 2H_2O$ (43 μmol) and polyvinyl alcohol (PVA, m[Au]/m[PVA] = 1:1) solution were added to 130 mL of DI water. After 3 min, 0.1 M $NaBH_4$ (n[$NaBH_4$]/ n[Au] = 4) solution was added to the yellow solution under vigorous magnetic stirring, resulting in the formation of a ruby red Au(0) sol. The fresh Au colloids (acidified at pH = 2 using H_2SO_4) were immobilized by adding the TiO_2 powders under vigorous stirring. The catalysts were filtered, washed on the filter, and dried at 80 °C for 4 h. The amount of Au was calculated to be 1 wt % Au/TiO_2 for both preparation methods. The Au/TiO_2 samples prepared by DP and SI methods are denoted as Au_{DP}/TiO_2 and Au_{SI}/TiO_2, respectively.

Catalyst Characterization. X-ray diffraction (XRD) was used to analyze the crystallinity and crystallite size of the samples by using an X-ray diffractometer (SmartLab, Rigaku) operating with Cu Kα radiation. A scan rate of 0.04° s^{-1} and integration time of 10.0 s were used for all measurements. The averaged crystallite size of TiO_2 was determined via Rietveld refinement of the diffraction patterns.[44,45] The crystallinity of the as-synthesized TiO_2 was analyzed by mixing the sample with a 100% crystalline CaF_2 reference in a 1:1 weight ratio. The crystallinity of the sample was then calculated by comparing the integrated peaks of anatase (101) and CaF_2 (111) using eq 1[46]

$$\text{crystallinity} = 0.763 \times A_{\text{anatase}(101)} / A_{CaF_2\,(111)} \times 100 \quad (1)$$

The loading of Au on each catalyst was determined by atomic absorption spectroscopy (AAS) using a PerkinElmer 3100 spectrometer. Samples for transmission electron micro-

scopic (TEM) characterization were prepared by drop-casting catalyst−ethanol suspensions on a holy carbon coated copper grid. An FEI Titan 80−300 kV TEM was used to obtain high-resolution images. The mean particle diameters of TiO_2 and Au NPs were calculated by analyzing 200 particles. X-ray photoelectron spectroscopy (XPS) analysis was carried out using a Kratos Axis Ultra spectrometer equipped with a monochromatic Al Kα source (10 mA, 15 kV). Pass energies of 40 and 160 eV were used for high-resolution scans and survey scans, respectively. The XPS spectra were calibrated using adventitious carbon (binding energy of C1s = 284.8 eV).

Catalytic Testing. Photocatalytic Performance. Photocatalytic H_2 evolution was investigated using glycerol as the scavenger. Prior to the experiment, the fresh photocatalyst (50 mg) was dispersed in 22.5 mL of DI water and cleaned by UV irradiation (Optimax 365, 365 nm LED, photon flux: 4×10^{17} photons s^{-1}) for 2 h to remove any surface adsorbed organic contaminations. 2.5 mL of glycerol was added to the reactor to form a 10 vol % glycerol−catalyst−water suspension (25 mL). The reactor was then connected to a quadruple mass spectrometer (QMS, Hiden HPR-20), and the partial pressures of m/z = 2 (H_2), 18 (H_2O), 28 (N_2), 32 (O_2), and 44 (CO_2) species were monitored in situ. Before irradiation, the reactor was evacuated via a by-pass pump to remove the O_2 (C[O_2] < 10 ppm). UV irradiation was then commenced for 2 h to initiate the photocatalytic H_2 evolution under room-temperature conditions using the same LED light source as described above. More details of the photoreactivity measurements and related calculations can be found in the Supporting Information.

Heterogeneous Liquid Phase Glycerol Oxidation. Glycerol (0.3 M) and the catalyst (n[glycerol]/n[metal] = 1000) were mixed in DI water (total volume of 10 mL) and 4 equiv of NaOH in the reactor, which was pressurized at 300 kPa N_2 at T = 50 °C. The gas supply was eventually switched to O_2 under vigorous stirring to initiate the reaction. Aliquots were extracted periodically and analyzed by a high-performance liquid chromatography (HPLC) using a column (Alltech OA-10308, 300 mm × 7.8 mm) with UV and refractive index (RI) detectors. Aqueous H_3PO_4 solution (0.1 wt %) was used as the eluent. Products were identified by comparing with standard samples.

Mechanism Analysis. In Situ UV−vis Analysis. The photoreduction of methylene blue (MB) was followed under deaerated conditions to evaluate the kinetics of photogenerated charge carriers and the apparent Fermi level (E_F) of all photocatalysts.[21] First, 100 mL of photocatalyst suspension (10 mg L^{-1}) was prepared, UV-cleaned for 2 h, and transferred to a homemade in situ UV−vis reactor.[47] Then 1 mL of MB (500 μM) was added into the suspension under vigorous stirring. The suspension was subsequently purged by N_2 continuously for 30 min under dark conditions. Meanwhile, the suspension was circulated using a macromagnetic stirrer that was placed under a flow-cell cuvette placed in a UV−vis spectrometer (UH-4150, Hitachi). UV irradiation was then commenced after the MB ad/desorption equilibrium was reached. Simultaneously, UV−vis spectra were recorded in situ at given time intervals for all samples. The characteristic absorption peak located at 664 nm is used to determine the evolution of MB. More details can be found in our previous work and the Supporting Information.[21,47]

Electrochemical Characterization. The cyclic voltammograms (CV) during glycerol oxidation were recorded by a potentiostat (AUTOLAB PGSTAT 30) using a three-electrode system. The Au/TiO_2 catalyst deposited on glassy carbon, a Pt mesh (99.99%, 25 × 25 mm, Advent), and a Ag|AgCl electrode (3 M KCl, Metrohm) were used as the working electrode (WE), counter electrode (CE), and reference electrode (RE), respectively. The electrolyte was 0.1 M NaOH. Prior to the CV analysis of glycerol oxidation, the Au/TiO_2 catalyst film was swept in the potential range of −0.3 to 0.6 V versus Ag|AgCl at a scan rate of 50 mV s^{-1} until stabilization. Then 5 mL of glycerol was added into the electrolyte to form a 10 vol % glycerol electrolyte. Glycerol oxidation was recorded in the range of −0.6 to 1.5 V versus Ag|AgCl with a scan rate of 10 mV s^{-1}. The CVs of all Au_{DP}/TiO_2 samples were also measured in a 1 M NaOH electrolyte (−0.8 to 1.0 V vs SHE) under both deaerated and aerated conditions using glassy carbon as the CE.

RESULTS AND DISCUSSION

Physical Properties. The as-synthesized TiO_2 powders solely consist of anatase, as evidenced by the XRD patterns shown in Figure 1a. Anatase TiO_2 powders with averaged

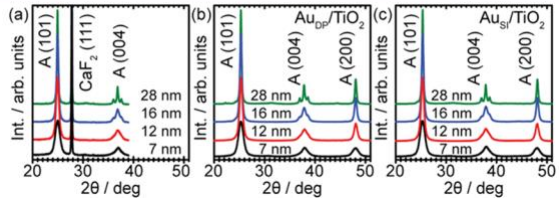

Figure 1. (a) XRD patterns of pristine TiO_2 with different crystallite sizes (7, 12, 16, 28 nm). Crystalline CaF_2 has been added to enable crystallinity analysis. (b,c) XRD patterns of Au NPs loaded on TiO_2 by DP and SI methods. The diffraction peaks of anatase (A) and CaF_2 are labeled.

crystallite sizes of 7, 12, 16, and 28 nm have been successfully synthesized, as confirmed by Rietveld refinement of the XRD patterns. In addition, the crystallinity of all samples is similar (>95%) according to eq 1. Figure 1b,c shows the XRD patterns of TiO_2 powders after loading with Au NPs via DP and SI methods, respectively. The XRD patterns for each sample show no obvious changes, suggesting that neither DP nor SI deposition affects the physical properties of the TiO_2 support. Diffraction peaks from the Au NPs cannot be detected due to a similar low loading of all Au/TiO_2 catalysts according to AAS analysis (~1 wt %, Table S2 in the Supporting Information).

TEM analysis reveals that the averaged particle sizes of the anatase TiO_2 supports after Au deposition are 6 ± 0.5, 10 ± 1, 17 ± 3, and 35 ± 10 nm for the 7, 12, 16, and 28 nm samples, respectively. The good agreement between the TEM and XRD analysis reveals that the TiO_2 particles show very low agglomeration. Figure 2 shows high-resolution TEM (HRTEM) images of Au NPs loaded on TiO_2 with different crystallite sizes via DP and SI methods. Mainly polycrystalline Au NPs are presented on the TiO_2 support, which is in good agreement with previous reports.[48,49] We have also analyzed the averaged particle sizes of Au NPs in all samples. While a similar particle size distribution with averaged particle size of approximately 4−6 nm is observed for the Au NPs supported on 7, 12, and 16 nm TiO_2 prepared by the DP method, Au particles of larger size (~12 nm) and a broader size distribution are observed for Au NPs supported on 28 nm TiO_2 via the DP method (Figure S3a in the Supporting

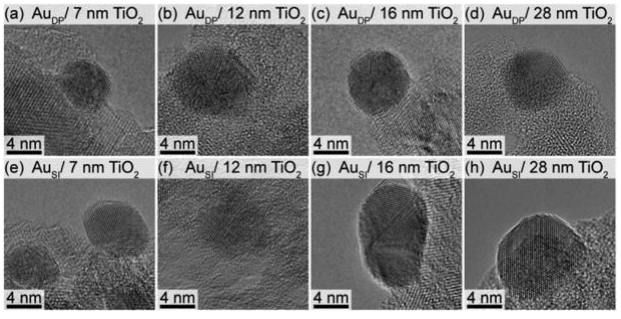

Figure 2. (a−d) HRTEM images of Au NPs deposited on TiO_2 with different crystallite sizes by DP method. (e−h) HRTEM images of Au NPs deposited on TiO_2 with different crystallite sizes by SI method.

Information). The larger size of Au NPs observed on 28 nm TiO_2 may result in a relatively poor performance in both photo- and electrocatalytic glycerol conversion. In comparison, the Au NPs supported on 12, 16, and 28 nm TiO_2 via the SI method show a similar size distribution with averaged particle size of approximately 4−6 nm (Figure S3b in the Supporting Information). We also noticed a slightly larger averaged particle size (~8 nm) and a broader size distribution of Au NPs supported on the 7 nm TiO_2. According to the TEM image of this material (Figure S2a in the Supporting Information), the large Au NPs (~8 nm) are supported on TiO_2 clusters that contain several small TiO_2 NPs (~7 nm). Therefore, we consider that the agglomeration of small TiO_2 enables the deposition of large Au NPs. Such a mismatch of the size may result in a weak interaction of the metal and TiO_2 support, thus resulting in a poor performance. In addition, elemental mapping of two representative Au/TiO_2 catalysts also shows that Au NPs are homogeneously deposited on TiO_2 (Figure S4 in the Supporting Information).

We have further examined the chemical composition of the Au/TiO_2 samples from both preparation methods using XPS. The survey scans reveal that all samples consist of Ti, O, C, and Au (Figure S5 in the Supporting Information). The deposition of Au shows a negligible impact on the oxidation state of Ti, as evidenced by the intense Ti^{4+} signals shown in the Ti2p spectra (Figure 3a).[50] Correspondingly, the high-resolution scan of Au4f indicates that all Au NPs are in their metallic form (Au4f$_{7/2}$ = 83.1 eV) regardless of the deposition methods and the TiO_2 support size (Figure 3c).[36] It is also

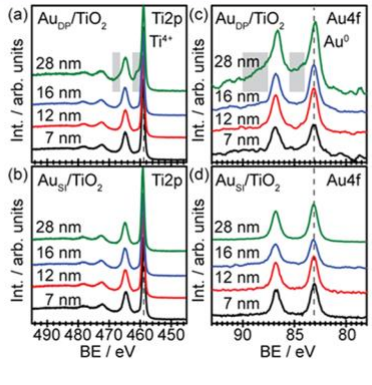

Figure 3. High-resolution XPS spectra of (a,b) Au4f and (c,d) Ti2p of Au NPs loaded on TiO_2 by DP and SI methods. The regions marked in gray indicate the possible peak broadening caused by the charging effect.

worth noting that a weak peak broadening caused by a charging effect is observed in both Ti2p and Au4f spectra of the Au deposited on 28 nm TiO_2 via the DP method (marked in gray). The charging effect arising from the insufficient neutralization of localized electrons may result from the large crystallite size of TiO_2 NPs that are insufficient in charge transfer compared to that of smaller TiO_2 NPs. However, this will not influence the oxidation state analysis of the material. Furthermore, all TiO_2 samples show a comparable Au4f/Ti2p ratio, suggesting a similar Au exposure on the TiO_2 surface with different crystallite sizes (Table S3 in the Supporting Information).

Catalytic Performance. According to previous investigation, the photoreforming of glycerol under deaerated conditions using metal/TiO_2 photocatalyst mainly follows the oxidative C−C cleavage process, resulting in the formation of glycolaldehyde and formaldehyde as the dominant species in the liquid phase.[10] Since both geometric and electronic structures of the metal cocatalyst strongly influence the reaction kinetics and selectivity in alcohol conversion,[21,50,51] we focus on the effect of the Au deposition method and TiO_2 crystallite size on the gas phase product(s) during photocatalytic glycerol reforming under deaerated conditions. Figure 4a depicts the time-resolved photocatalytic H_2 evolution using

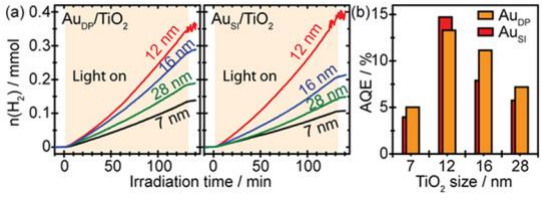

Figure 4. (a) In situ profiles of photocatalytic H_2 evolution from aqueous glycerol solution (25 vol %) using Au NPs deposited on TiO_2 with different crystallite sizes by DP and SI methods. (b) Comparison of AQE of photocatalytic H_2 evolution using different photocatalysts. The pristine TiO_2 show no activity.[54]

all photocatalysts under UV irradiation. A significant enhancement in H_2 evolution is observed upon increase in the crystallite size of TiO_2 from 7 to 12 nm, and a further increase in crystallite size results in a reduction of the H_2 evolution rate. Interestingly, this trend is independent of the deposition methods. We have also evaluated the reusability of two representative samples, both of which show excellent stability within four consecutive cycles (Figure S6 in the Supporting Information). To further evaluate the effect of the deposition method on the photocatalytic performance, we have plotted the apparent quantum efficiency (AQE) as a function of the TiO_2 crystallite size for both deposition methods, as demonstrated in Figure 4b. Similar AQE values are observed for the Au$_{DP}$ and Au$_{SI}$ deposited on TiO_2 with the same crystallite size, suggesting that, although there is some variation in the particle size of Au, the deposition methods show a weak influence on the photocatalytic performance compared to that of the crystallite size of TiO_2. Additionally, our Au/TiO_2 photocatalyst shows an optimum quantum efficiency of ~15%, which is comparable to reported values of Au/TiO_2 samples.[52,53] The promotion mechanisms will be discussed in detail in the Mechanistic Studies section.

We have further studied the thermal oxidation of glycerol using all Au/TiO_2 catalysts, as presented in Figure 5. Although glycerol is mainly converted to glycerate with a selectivity of

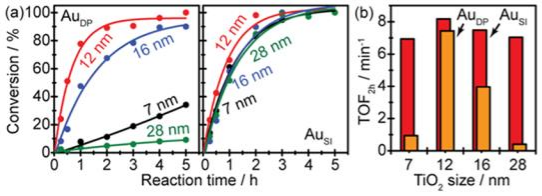

Figure 5. (a) Heterogeneous glycerol oxidation using Au NPs deposited on TiO_2 with different crystallite sizes by DP and SI methods. (b) Comparison of TOF of glycerol oxidation using different catalysts.

approximately 70−80% (Table S4 in the Supporting Information) for the whole series of Au/TiO_2 samples regardless of the deposition method, the conversion efficiency is strongly dependent on both metal deposition method and crystallite size, as demonstrated in Figure 5a. While a similar optimum catalytic performance is observed at the Au supported on 12 nm TiO_2 for both deposition methods, a large deviation in efficiency is noted for Au supported on TiO_2 via the direct precipitation process compared to that of the sol-immobilization process. All catalysts present an exponential conversion of glycerol, which suggests a pseudo-first-order reaction kinetics, though two of the Au_{DP}/TiO_2 samples (with 7 and 28 nm TiO_2) show very slow reaction rates. The turnover frequencies after 2 h of reaction (TOF_{2h}) of all samples are demonstrated in Figure 5b for better comparison. For the Au_{DP}/TiO_2 catalysts, a 7-fold enhancement is observed by increasing the TiO_2 support from 7 to 12 nm. A further increment in the size of TiO_2 results in a significant drop of the performance, and the catalyst becomes almost inactive when the size of TiO_2 reaches 28 nm. Although a similar trend in the catalytic performance is observed for the Au_{SI}/TiO_2 series, the variation in performance is insignificant. In addition, the optimized TOF observed for Au_{SI}/TiO_2 (12 nm) is 3 times better than that of Au_{SI} supported on Degussa P25 and is comparable to that of Au supported on activated carbon.[6,38] Although Au NPs are the active species for thermal catalytic glycerol conversion, the metal−support interaction strongly influences the catalytic performance. Generally, the promotional effect is considered to be linked to the optimized particle size of Au NPs; however, it is still unclear from a reaction kinetic level. Therefore, we have further investigated the promotional mechanisms by employing electrochemical analysis in detail in the Mechanistic Studies section.

Mechanistic Studies. Previous investigation on Au-Pd bimetallic NPs supported on TiO_2 reveals that tuning the kinetics of charge carriers is crucial in optimizing the photocatalytic H_2 evolution performance.[21] Therefore, we anticipate that the variation in both deposition method and crystallite size of TiO_2 influences the charge carrier kinetics and thus the photocatalytic performance. Figure 6a,b compares the in situ UV−vis spectroscopy recorded during methylene blue (MB) reduction under deaerated conditions using selected Au/TiO_2 photocatalysts. Note that the bleaching of MB molecules to its MB^{2-} anion can be used to titrate the number of effective photogenerated electrons and the kinetics of the charge carriers,[21,25] as depicted in the following equation:

$$2MB + 2e^-_{CB} \xrightarrow{h\nu, N_2, \text{photocat}} 2MB^{-\cdot} \rightarrow MB + MB^{2-}(\text{colorless}) \quad (2)$$

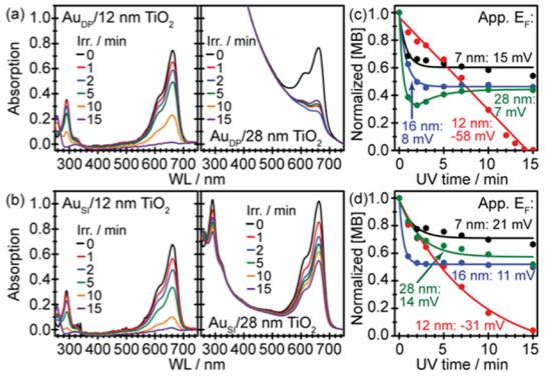

Figure 6. (a,b) Representative in situ UV−vis spectra recorded during photocatalytic MB reduction under deaerated conditions using Au NPs loaded on TiO_2 by DP and SI methods. (c,d) Time profiles of photocatalytic MB reduction using Au NPs loaded on TiO_2 by DP and SI methods.

While the Au_{DP} NPs supported on 12 nm TiO_2 show a gradual depletion of MB to almost zero upon irradiation, the Au_{DP} NPs supported on 28 nm TiO_2 show a much more rapid initial depletion rate after which the remaining MB reaches an equilibrium (Figure 6a). The Au_{SI} NPs supported on 12 nm TiO_2 shows a similar trend to Au_{DP} NPs on the same TiO_2, whereas the Au_{SI} NPs supported on 28 nm TiO_2 show a much slower reduction of MB.

We have further plotted the evolution of MB as a function of irradiation time to rationalize the effect of deposition methods and TiO_2 crystallite size, as shown in Figure 6c,d. Furthermore, the apparent Fermi levels (E_F) of all Au/TiO_2 have also been estimated by employing the Nernst equation

$$E_F = E^0 + \frac{0.059}{2} \times \log([MB] / [MB^{2-}]) \quad (3)$$

where E^0 is the two-electron redox potential of the MB/MB^{2-} couple (0.01 V vs SHE). For all Au_{DP}/TiO_2 samples, the photoreduction of MB follows an exponential decay and reaches equilibrium except for the Au_{DP} on 12 nm TiO_2, suggesting pseudo-first-order reaction kinetics where the photoreduction is limited by the number of excited electrons. Although the depletion rate of MB using Au_{DP} on 12 nm TiO_2 is slow, the near complete reduction of MB suggests a significant shift of E_F (−58 mV vs SHE) compared to those for the rest of the Au_{DP}/TiO_2 photocatalysts, thus revealing a more reductive energy level of the photocatalyst system that is beneficial for photocatalytic hydrogen reduction. Similarly, the high photocatalytic performance of Au_{SI} NPs supported on 12 nm TiO_2 in comparison to the rest of the Au_{SI}/TiO_2 photocatalysts can also be contributed to the more negative E_F (−31 mV vs SHE).

Since the photocatalytic glycerol reforming and the heterogeneous thermal catalytic oxidation of glycerol are carried out under different reaction conditions (neutral pH and deaerated conditions vs basic and aerated conditions), we believe that the promotion mechanisms are different. Therefore, we have employed electrochemical analysis to probe the possible promotion effect in the glycerol thermal oxidation under alkaline conditions. Compared to other ex situ characterization techniques, the electrochemical CV analyses allow us to investigate both oxidation and reduction half-reactions in glycerol oxidation under reaction conditions.

Figure 7a first presents the CV profiles of all Au/TiO_2 catalysts prepared by the DP method in the 0.1 M NaOH

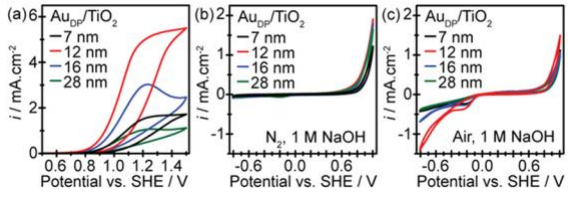

Figure 7. (a) CV profiles of glycerol electrooxidation using Au NPs loaded on TiO_2 with different crystallite sizes by DP methods. The electrolyte was 0.1 M NaOH with 10 vol % glycerol. (b,c) CV profiles of Au_{DP}/TiO_2 in 1 M NaOH measured under deaerated conditions and aerated conditions, respectively.

electrolyte in the presence of 10 vol % glycerol under ambient conditions. All Au/TiO_2 catalysts show activity in electrochemical oxidation of glycerol with the Au on 12 nm TiO_2 yielding the highest activity (onset potential at ~0.9 V vs SHE). The activity of the Au/TiO_2 catalysts also shows a similar size-dependent trend to that observed in thermal glycerol oxidation (12 > 16 > 7 > 28 nm). Furthermore, all Au/TiO_2 catalysts provide very similar electrooxidation curves, confirming that all catalysts exhibit a similar selectivity that agrees well with the thermal catalytic performance. No gas evolution was observed below 1.4 V versus SHE, indicating that the water oxidation is negligible.

We have further probed the mechanisms by CV analysis in 1 M NaOH under aerated and deaerated conditions. As presented in Figure 7b, all Au_{DP}/TiO_2 catalysts show similar CV profiles, revealing that the glycerol conversion is not limited by the oxidative capacity of the catalyst. The Au NPs supported on TiO_2 with different sizes exhibit distinct CV profiles in the negative potential range under aerated conditions, as demonstrated in Figure 7c. The Au_{DP} NPs supported on the 12 nm TiO_2 show a much higher current density than the other catalysts, suggesting a superior oxygen reduction performance.[55,56] The electrochemical oxygen reduction activity of the Au_{DP}/TiO_2 samples is size-dependent and follows the order of 12 > 16 > 7 > 28 nm, which agrees well with both thermal and electrochemical oxidation of glycerol. Therefore, it suggests that the Au on medium-sized TiO_2 promotes the aerobic glycerol oxidation by accelerating the oxygen reduction half-reaction. In addition, CV analysis of a representative Au_{SI}/TiO_2 catalyst (12 nm TiO_2) also confirms that the oxygen reduction half-reaction determines the overall performance in glycerol oxidation (Figure S7 in the Supporting Information).

CONCLUSIONS

Here, we have studied the promotional mechanisms of Au supported on TiO_2 in photo- and thermal catalytic glycerol reforming. Gold NPs have been loaded on a series of anatase TiO_2 supports with different crystallite sizes (7, 12, 16, 28 nm) by both direct precipitation and sol-immobilization methods. For photocatalytic H_2 evolution from glycerol, a similar optimum performance was observed for the Au on 12 nm TiO_2 regardless of the Au deposition method. In situ UV−vis spectrometry reveals that the optimized photocatalytic performance originated from an enhanced charge separation and a more negative Fermi level for proton reduction. For thermal catalytic glycerol oxidation, although an optimum performance was observed for the Au supported on 12 nm TiO_2, the metal deposition method significantly influences the catalytic activity. Electrochemical analysis reveals that the enhanced glycerol oxidation can be assigned to the enhanced oxygen reduction power.

ASSOCIATED CONTENT

* Supporting Information

The Supporting Information is available free of charge on the ACS Publications website at DOI: 10.1021/acs.jpcc.9b05475.

Experimental details, TEM images of the Au/TiO_2 samples, and HPLC analysis of the glycerol oxidation products (PDF)

AUTHOR INFORMATION

Corresponding Authors

*E-mail: alberto.villa@unimi.it (A.V.).

*E-mail: suren@synfuelschina.com.cn (R.S.).

ORCID

Xi Liu: 0000-0002-8654-0774

Tommaso Tabanelli: 0000-0003-0616-8990

Bo B. Iversen: 0000-0002-4632-1024

Laura Prati: 0000-0002-8227-9505

Graham Hutchings: 0000-0001-8885-1560

Ren Su: 0000-0002-1423-6431

Present Address

¶Suzhou Institute of Nano-Tech and Nano-Bionics (SINANO), No. 398 Ruoshui Road, Suzhou Industrial Park, Suzhou, 215123, China (Y.S.).

Author Contributions

Y.S. and R.S. conceived the studies. A.M., N.D., and A.V. synthesized the samples; Y.S. and R.S. performed the photocatalytic tests; A.V. carried out the thermal catalytic tests; R.S. performed the mechanistic studies; A.M., X.L., T.W.H., and T.T. performed material characterizations. All authors were involved in the design of the experiments, the discussion of the results, and the writing of the manuscript. The manuscript was written through contributions of all authors. All authors have given approval to the final version of the manuscript.

Notes

The authors declare no competing financial interest.

ACKNOWLEDGMENTS

R.S. and Y.S. thank financial support from the NSFC (project numbers: 21503257, 21673236) and the Beijing Overseas Talents Association (BOTA). A.M. and B.B.I. acknowledge support from the Danish National Research Foundation (DNRF93).

REFERENCES

(1) San Kong, P.; Aroua, M. K.; Daud, W. M. A. W. Conversion of crude and pure glycerol into derivatives: A feasibility evaluation. Renewable Sustainable Energy Rev. 2016, 63, 533−555.

(2) Ott, L.; Bicker, M.; Vogel, H. Catalytic dehydration of glycerol in sub- and supercritical water: a new chemical process for acrolein production. Green Chem. 2006, 8, 214−220.

(3) Dow Chemical New propylene glycol provides environmental benefits, reliable performance and competitive economics, 2007, https:// www.chemeurope.com/en/news/62841/dow-achieves-another-major-milestone-in-its-quest-for-sustainable-chemistries.html.

(4) Pagliaro, M.; Ciriminna, R.; Kimura, H.; Rossi, M.; Della Pina, C. From glycerol to value-added products. Angew. Chem., Int. Ed. 2007, 46, 4434−4440.
(5) Melero, J. A.; van Grieken, R.; Morales, G.; Paniagua, M. Acidic mesoporous silica for the acetylation of glycerol: synthesis of bioadditives to petrol fuel. Energy Fuels 2007, 21, 1782−1791.
(6) Wang, D.; Villa, A.; Su, D.; Prati, L.; Schlögl, R. Carbon-supported gold nanocatalysts: shape effect in the selective glycerol oxidation. ChemCatChem 2013, 5, 2717−2723.
(7) Zhang, Z.; Xin, L.; Qi, J.; Chadderdon, D. J.; Sun, K.; Warsko, K. M.; Li, W. Selective electro-oxidation of glycerol to tartronate or mesoxalate on Au nanoparticle catalyst via electrode potential tuning in anion-exchange membrane electro-catalytic flow reactor. Appl. Catal., B 2014, 147, 871−878.
(8) Zope, B. N.; Hibbitts, D. D.; Neurock, M.; Davis, R. J. Reactivity of the gold/water interface during selective oxidation catalysis. Science 2010, 330, 74−78.
(9) Zhang, Y.; Zhang, N.; Tang, Z.-R.; Xu, Y.-J. Identification of Bi_2WO_6 as a highly selective visible-light photocatalyst toward oxidation of glycerol to dihydroxyacetone in water. Chem. Sci. 2013, 4, 1820−1824.
(10) Sanwald, K. E.; Berto, T. F.; Eisenreich, W.; Gutierrez,́ O. Y.; Lercher, J. A. Catalytic routes and oxidation mechanisms in photoreforming of polyols. J. Catal. 2016, 344, 806−816.
(11) Christoph, R.; Schmidt, B.; Steinberner, U.; Dilla, W.; Karinen, R. Glycerol. Ullmann's Encyclopedia of Industrial Chemistry; Wiley− VCH Verlag GmbH & Co. KGaA: 2006.
(12) Jin, X.; Zhao, M.; Zeng, C.; Yan, W.; Song, Z.; Thapa, P. S.; Subramaniam, B.; Chaudhari, R. V. Oxidation of Glycerol to Dicarboxylic Acids Using Cobalt Catalysts. ACS Catal. 2016, 6, 4576−4583.
(13) Villa, A.; Dimitratos, N.; Chan-Thaw, C. E.; Hammond, C.; Prati, L.; Hutchings, G. J. Glycerol oxidation using gold-containing catalysts. Acc. Chem. Res. 2015, 48, 1403−1412.
(14) Hu, W.; Knight, D.; Lowry, B.; Varma, A. Selective oxidation of glycerol to dihydroxyacetone over Pt−Bi/C catalyst: optimization of catalyst and reaction conditions. Ind. Eng. Chem. Res. 2010, 49, 10876−10882.
(15) Villa, A.; Campisi, S.; Chan-Thaw, C. E.; Motta, D.; Wang, D.; Prati, L. Bismuth modified Au-Pt bimetallic catalysts for dihydroxyacetone production. Catal. Today 2015, 249, 103−108.
(16) Ning, X.; Li, Y.; Yu, H.; Peng, F.; Wang, H.; Yang, Y. Promoting role of bismuth and antimony on Pt catalysts for the selective oxidation of glycerol to dihydroxyacetone. J. Catal. 2016, 335, 95− 104.
(17) Yang, L.; Li, X.; Sun, Y.; Yue, L.; Fu, J.; Lu, X.; Hou, Z. Selective oxidation of glycerol in base-free conditions over N-doped carbon film coated carbon supported Pt catalysts. Catal. Commun. 2017, 101, 107−110.
(18) Kondrat, S. A.; Miedziak, P. J.; Douthwaite, M.; Brett, G. L.; Davies, T. E.; Morgan, D. J.; Edwards, J. K.; Knight, D. W.; Kiely, C. J.; Taylor, S. H.; Hutchings, G. J. Base-free oxidation of glycerol using titania-supported trimetallic Au−Pd−Pt nanoparticles. ChemSusChem 2014, 7, 1326−1334.
(19) Chong, R.; Li, J.; Zhou, X.; Ma, Y.; Yang, J.; Huang, L.; Han, H.; Zhang, F.; Li, C. Selective photocatalytic conversion of glycerol to hydroxyacetaldehyde in aqueous solution on facet tuned TiO_2-based catalysts. Chem. Commun. 2014, 50, 165−167.
(20) Chen, W.-T.; Chan, A.; Al-Azri, Z. H. N.; Dosado, A. G.; Nadeem, M. A.; Sun-Waterhouse, D.; Idriss, H.; Waterhouse, G. I. N. Effect of TiO_2 polymorph and alcohol sacrificial agent on the activity of Au/TiO_2 photocatalysts for H_2 production in alcohol−water mixtures. J. Catal. 2015, 329, 499−513.
(21) Su, R.; Tiruvalam, R.; Logsdail, A. J.; He, Q.; Downing, C. A.; Jensen, M. T.; Dimitratos, N.; Kesavan, L.; Wells, P. P.; Bechstein, R.; et al. Designer titania-supported Au-Pd nanoparticles for efficient photocatalytic hydrogen production. ACS Nano 2014, 8, 3490−3497.
(22) Jones, W.; Su, R.; Wells, P. P.; Shen, Y.; Dimitratos, N.; Bowker, M.; Morgan, D.; Iversen, B. B.; Chutia, A.; Besenbacher, F.; et al. Optimised photocatalytic hydrogen production using core-shell AuPd promoters with controlled shell thickness. Phys. Chem. Chem. Phys. 2014, 16, 26638−26644.
(23) Hang Li, Y.; Xing, J.; Jia Chen, Z.; Li, Z.; Tian, F.; Rong Zheng, L.; Feng Wang, H.; Hu, P.; Jun Zhao, H.; Gui Yang, H. Unidirectional suppression of hydrogen oxidation on oxidized platinum clusters. Nat. Commun. 2013, 4, 2500.
(24) Yang, J.; Wang, D.; Han, H.; Li, C. Roles of cocatalysts in photocatalysis and photoelectrocatalysis. Acc. Chem. Res. 2013, 46, 1900−1909.
(25) Takai, A.; Kamat, P. V. Shuttling photogenerated electrons across TiO_2-silver interface. ACS Nano 2011, 5, 7369−7376.
(26) Kim, M.; Lee, H. Highly Selective production of acrylic acid from glycerol via two steps using Au/CeO_2 catalysts. ACS Sustainable Chem. Eng. 2017, 5, 11371−11376.
(27) Liu, S.-S.; Sun, K.-Q.; Xu, B.-Q. Specific selectivity of Au-catalyzed oxidation of glycerol and other C_3-polyols in water without the presence of a base. ACS Catal. 2014, 4, 2226−2230.
(28) Bowker, M.; Davies, P. R.; Al-Mazroai, L. S. Photocatalytic reforming of glycerol over gold and palladium as an alternative fuel source. Catal. Lett. 2009, 128, 253.
(29) Li, M.; Li, Y.; Peng, S.; Lu, G.; Li, S. Photocatalytic hydrogen generation using glycerol wastewater over Pt/TiO_2. Front. Chem. China 2009, 4, 32−38.
(30) Ou, M.; Wan, S.; Zhong, Q.; Zhang, S.; Wang, Y. Single Pt atoms deposition on g-C_3N_4 nanosheets for photocatalytic H_2 evolution or NO oxidation under visible light. Int. J. Hydrogen Energy 2017, 42, 27043−27054.
(31) Guo, L.; Sun, Q.; Marcus, K.; Hao, Y.; Deng, J.; Bi, K.; Yang, Y. Photocatalytic glycerol oxidation on Au_xCu−CuS@TiO_2 plasmonic heterostructures. J. Mater. Chem. A 2018, 6, 22005.
(32) Kwon, Y.; Schouten, K. J. P.; Koper, M. T. M. Mechanism of the catalytic oxidation of glycerol on polycrystalline gold and platinum electrodes. ChemCatChem 2011, 3, 1176−1185.
(33) Panagiotopoulou, P.; Karamerou, E. E.; Kondarides, D. I. Kinetics and mechanism of glycerol photo-oxidation and photo-reforming reactions in aqueous TiO_2 and Pt/TiO_2 suspensions. Catal. Today 2013, 209, 91−98.
(34) Namdeo, A.; Mahajani, S. M.; Suresh, A. K. Palladium catalysed oxidation of glycerol effect of catalyst support. J. Mol. Catal. A 2016, 421, 45−56.
(35) Su, R.; Dimitratos, N.; Liu, J.; Carter, E.; Althahban, S.; Wang, X.; Shen, Y.; Wendt, S.; Wen, X.; Niemantsverdriet, J. W.; et al. Mechanistic insight into the interaction between a titanium dioxide photocatalyst and Pd cocatalyst for improved photocatalytic perform-ance. ACS Catal. 2016, 6, 4239−4247.
(36) Su, R.; Forde, M. M.; He, Q.; Shen, Y.; Wang, X.; Dimitratos, N.; Wendt, S.; Huang, Y.; Iversen, B. B.; Kiely, C. J.; et al. Well-controlled metal co-catalysts synthesised by chemical vapour impregnation for photocatalytic hydrogen production and water purification. Dalton Trans. 2014, 43, 14976−14982.
(37) D'Agostino, C.; Brett, G.; Divitini, G.; Ducati, C.; Hutchings, G. J.; Mantle, M. D.; Gladden, L. F. Increased affinity of small gold particles for glycerol oxidation over Au/TiO_2 probed by NMR relaxation methods. ACS Catal. 2017, 7, 4235−4241.
(38) Villa, A.; Wang, D.; Su, D. S.; Prati, L. Gold sols as catalysts for glycerol oxidation: the role of stabilizer. ChemCatChem 2009, 1, 510− 514.
(39) Zhang, C.; Wang, T.; Ding, Y. Influence of Pt particle size on the activity of Pt/AC catalyst in selective oxidation of glycerol to lactic acid. Catal. Lett. 2017, 147, 1197−1203.
(40) Li, Y.; Zaera, F. Sensitivity of the glycerol oxidation reaction to the size and shape of the platinum nanoparticles in Pt/SiO_2 catalysts. J. Catal. 2015, 326, 116−126.
(41) Kwon, Y.; Lai, S. C. S.; Rodriguez, P.; Koper, M. T. M. Electrocatalytic oxidation of alcohols on gold in alkaline media: base or gold Catalysis? J. Am. Chem. Soc. 2011, 133, 6914−6917.
(42) Hald, P.; Becker, J.; Bremholm, M.; Pedersen, J. S.; Chevallier, J.; Iversen, S. B.; Iversen, B. B. Supercritical propanol−water synthesis

and comprehensive size characterisation of highly crystalline anatase TiO_2 nanoparticles. J. Solid State Chem. 2006, 179, 2674−2680.
(43) Mi, J.-L.; Johnsen, S.; Clausen, C.; Hald, P.; Lock, N.; Søgaard, M.; Iversen, B. B. Highly controlled crystallite size and crystallinity of pure and iron-doped anatase-TiO_2 nanocrystals by continuous flow supercritical synthesis. J. Mater. Res. 2013, 28, 333−339.
(44) Wang, X.; Søgaard, M.; Su, R.; Wendt, S.; Hald, P.; Mamakhel, A.; Yang, C.; Huang, Y.; Iversen, B. B.; Besenbacher, F. The influence of crystallite size and crystallinity of anatase nanoparticles on the photo-degradation of phenol. J. Catal. 2014, 310, 100−108.
(45) Rietveld, H. M. A profile refinement method for nuclear and magnetic structures. J. Appl. Crystallogr. 1969, 2, 65−71.
(46) Jensen, H.; Joensen, K. D.; Jørgensen, J.-E.; Pedersen, J. S.; Søgaard, G. Characterization of nanosized partly crystalline photo-catalysts. J. Nanopart. Res. 2004, 6, 519−526.
(47) Su, R.; Kesavan, L.; Jensen, M. M.; Tiruvalam, R.; He, Q.; Dimitratos, N.; Wendt, S.; Glasius, M.; Kiely, C. J.; Hutchings, G. J.; et al. Selective photocatalytic oxidation of benzene for the synthesis of phenol using engineered Au-Pd alloy nanoparticles supported on titanium dioxide. Chem. Commun. 2014, 50, 12612−12614.
(48) Lopez-Sanchez, J. A.; Dimitratos, N.; Hammond, C.; Brett, G. L.; Kesavan, L.; White, S.; Miedziak, P.; Tiruvalam, R.; Jenkins, R. L.; Carley, A. F.; et al. Facile removal of stabilizer-ligands from supported gold nanoparticles. Nat. Chem. 2011, 3, 551−556.
(49) Tiruvalam, R. C.; Pritchard, J. C.; Dimitratos, N.; Lopez-Sanchez, J. A.; Edwards, J. K.; Carley, A. F.; Hutchings, G. J.; Kiely, C. J. Aberration corrected analytical electron microscopy studies of sol-immobilized Au + Pd, Au{Pd} and Pd{Au} catalysts used for benzyl alcohol oxidation and hydrogen peroxide production. Faraday Discuss. 2011, 152, 63−86.
(50) Jin, X.; Li, C.; Xu, C.; Guan, D.; Cheruvathur, A.; Wang, Y.; Xu, J.; Wei, D.; Xiang, H.; Niemantsverdriet, J. W.; et al. Photocatalytic C-C bond cleavage in ethylene glycol on TiO_2: A molecular level picture and the effect of metal nanoparticles. J. Catal. 2017, 354, 37−45.
(51) Kamat, P. V.; Jin, S. Semiconductor Photocatalysis: "Tell us the complete story!". ACS Energy Lett. 2018, 3, 622−623.
(52) Qian, K.; Huang, W. A new strategy to enhance quantum efficiency of photo-mediated hydrogen evolution. Catal. Today 2019, 327, 334−339.
(53) Elkoro, A.; Soler, L.; Llorca, J.; Casanova, I. 3D printed microstructured Au/TiO_2 catalyst for hydrogen photoproduction. Appl. Mater. Today 2019, 16, 265−272.
(54) Bamwenda, G. R.; Tsubota, S.; Nakamura, T.; Haruta, M. Photoassisted hydrogen-production from A water-ethanol solution - a comparison of activities of Au-TiO_2 and Pt-TiO_2. J. Photochem. Photobiol. A Chem. 1995, 89, 177−189.
(55) Sheng, H.; Ji, H.; Ma, W.; Chen, C.; Zhao, J. Direct four-electron reduction of O_2 to H_2O on TiO_2 surfaces by pendant proton relay. Angew. Chem., Int. Ed. 2013, 52, 9686−9690.
(56) Li, M. F.; Liao, L. W.; Yuan, D. F.; Mei, D.; Chen, Y.-X. pH effect on oxygen reduction reaction at Pt(111) electrode. Electrochim. Acta 2013, 110, 780−789.